

Article

Investigation of Electromagnetic Angle Sensor Integrated in FR4-Based Scanning Micromirror

Quan Wen ^{1,3}, Hongjie Lei ^{1,*}, Fan Yu ¹, Dongling Li ¹, Yin She ¹, Jian Huang ^{1,2},
Liangkun Huang ¹ and Zhiyu Wen ¹

¹ Key Laboratory of Fundamental Science of Micro/Nano-Device and System Technology, College of Optoelectronic Engineering, Chongqing University, Chongqing 400044, China; Quan.Wen@enas.fraunhofer.de (Q.W.); Yu_Fan@cqu.edu.cn (F.Y.); lidongling@cqu.edu.cn (D.L.); sheyin@cqu.edu.cn (Y.S.); huangjian7@gmail.com (J.H.); Huang_lk@cqu.edu.cn (L.H.); wzy@cqu.edu.cn (Z.W.)

² College of Information Engineering, Qujing Normal University, Qujing 655000, China

³ Fraunhofer Institute for Electronic Nano Systems (ENAS), 09126 Chemnitz, Germany

* Correspondence: leihongjie@cqu.edu.cn; Tel.: +86-023-6511-1010

Received: 5 November 2018; Accepted: 26 November 2018; Published: 28 November 2018



Abstract: This paper performs a detailed investigation on the electromagnetic angle sensor integrated in the flame retardant 4 (FR4)-based scanning micromirror. An accurate theoretical model is presented, especially considering the coupling effect between the driving and sensing coils. Experimental results agree well with the theoretical results, and show a sensitivity of 55.0 mV_p/° and a high signal-to-noise ratio (SNR) of 71.9 dB. Moreover, the linearity of the angle sensor can still reach 0.9995, though it is affected slightly by the coupling effect. Finally, the sensor's good feasibility for feedback control has been further verified through a simple closed-loop control circuit. The micromirror operated with closed-loop control possesses better long-term stability and temperature stability than that operated without closed-loop control.

Keywords: integrated angle sensor; electromagnetic; coupling effect; scanning micromirror; closed-loop control; flame retardant 4 (FR4)

1. Introduction

Scanning micromirrors are essential core elements in various optical microsystems (e.g., barcode reader, endoscopic probe, and LiDAR) [1–4]. Especially, a large-aperture and low-frequency micromirror is required for a broad range of applications, such as fluorescence microscopes [5], laser projection [6,7], micro-spectrometers [8–10], etc. However, conventional Si-based MEMS (microelectromechanical systems) micromirrors cannot meet the requirements because large-aperture and low-frequency Si micromirrors are fragile, and cannot survive the environmental shocks and vibrations [8,11]. In comparison, flame retardant 4 (FR4)-based micromirrors are more promising, due to the inherent flexibility of FR4 [7,12–14]. Until now, FR4 is the most widely used material for printed circuit boards (PCBs). Thus, commercial PCB technology, with low cost and a short process cycle, can be employed to fabricate the flexure and driving parts. After that, a mirror plate fabricated by dicing an aluminum-coated Si wafer is bonded to achieve large aperture and high surface quality. In general, the micromirror must scan the optical beam at a specific optical scan angle in practical applications. However, the current FR4 micromirror with a simple open-loop control cannot guarantee it, owing to the relatively poor stability of FR4 [12,15]. Therefore, an angle sensor is highly desired to monitor the scan angle in real time, and further form a feedback control.

External optical sensors may be a good solution to provide a real-time feedback signal [4,16,17]. However, this requires a complex assembly, and inevitably increases the system's volume and cost.

Another simple, yet highly effective alternative, is the integrated angle sensor. Several corresponding sensing methods have already been proposed and applied in MEMS micromirrors, such as piezoresistive [18,19], capacitive [20], piezoelectric [21,22], and electromagnetic [9,23]. Among these methods, electromagnetic angle sensing is more suitable to be integrated in the aforementioned FR4 micromirror, due to its excellent process compatibility. In our previous work [15], we presented a FR4-based electromagnetic scanning micromirror monolithically integrated with an electromagnetic angle sensor. However, it focused more on basic prototyping, driving performance, and reliability of the micromirror. As a continuation of previous work, this paper performed accurate modeling and detailed tests of the integrated angle sensor. Particularly, we study the coupling effect between the driving coil and sensing coil, which has not been reported by other groups, up to now. Finally, a simple closed-loop control circuit is developed to further verify the angle sensor's good feasibility for providing a real-time feedback signal.

This paper is organized as follows. Section 2 introduces the working principle of the electromagnetic angle sensor integrated in the FR4 micromirror, and presents the modeling. Section 3 discusses the test results and compares it with model results. Furthermore, the frequency response and phase-frequency characteristics of the angle sensor, and the closed-loop control, are also described in this section. The conclusion is summarized in Section 4.

2. Principle and Modeling

Figure 1a shows the schematic drawing of the assembled FR4 micromirror integrated with angle sensor. The device comprises a FR4 platform, a 11.7 mm × 10.3 mm aluminum-coated silicon mirror plate on it, a pair of permanent magnets assembled in parallel, and the package structure (i.e., the coverplate and baseplate). The thicknesses of the FR4 platform and silicon mirror plate are 0.4 mm and 0.5 mm, respectively. The layout of the FR4 platform is illustrated in Figure 1b. The inner sensing coil (double-layer planar Cu coil) and outer driving coil (single-layer planar Cu coil) are simultaneously integrated into the platform. When a driving signal with the resonant frequency (361.8 Hz) of the micromirror is applied in the driving coil, the generated Lorentz force will actuate the mirror to oscillate around the torsion bars at resonance. At the same time, an electromotive force is induced in the sensing coil. Therefore, the induced electromotive can be read out as a sensor signal for monitoring the variation of the deflection angle.

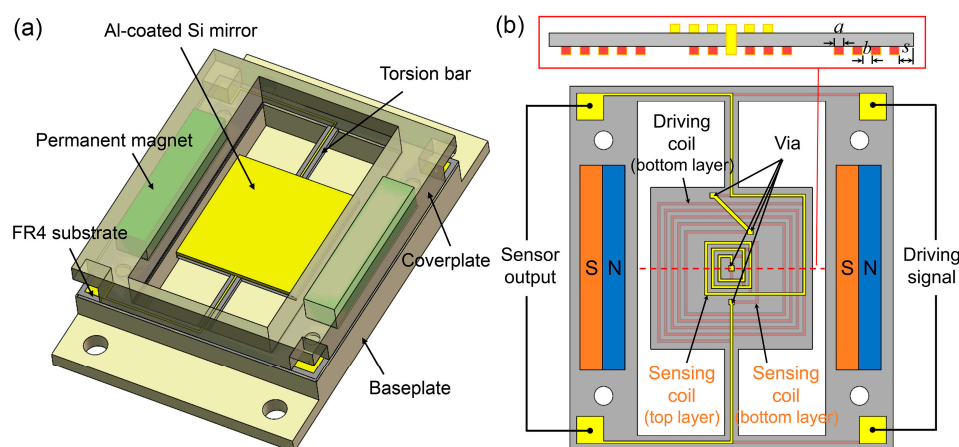


Figure 1. (a) Schematic drawing of the assembled FR4-based electromagnetic scanning micromirror integrated with angle sensor. (b) Layout of the integrated sensing coil in the FR4 platform.

The motion (mechanical half deflection angle θ) of the oscillating micromirror can be expressed by the following dynamical equation:

$$J_m \ddot{\theta} + C \dot{\theta} + K \theta = T, \quad (1)$$

where J_m , C , K , and T represent the moment of inertia of the platform with Si mirror plate, the damping coefficient, the torsion stiffness of torsion bars, and the driving torque, respectively.

As a sinusoidal driving voltage signal, $U_d = U_{d0}\sin\omega t$ is applied in the driving coil, and the corresponding driving current I_d is

$$I_d = \frac{U_d}{\sqrt{R_d^2 + (\omega L_d)^2}} = \frac{U_{d0}}{\sqrt{R_d^2 + (\omega L_d)^2}} \sin \omega t, \tag{2}$$

where R_d and L_d represent the resistance and inductance of the driving coil, respectively. Thus, the driving torque can be described as

$$T = I_d B M_d, \tag{3}$$

where B is the magnetic flux density produced by the magnets; M_d is identified as the area sum of all the driving coil, and it can be calculated from

$$M_d = \sum_{n=1}^{N_d} \left(\frac{w-2s-b}{2} - (n-1)(a+b) \right) \cdot ((2l-4s-3a-5b) - 4(n-1)(a+b)) - \left(\frac{w-2s-b}{2} - (N_d-1)(a+b) \right) \cdot ((l-2s-2a-3b) - 2(N_d-1)(a+b)), \tag{4}$$

where N_d is the number of the driving coil turns, l and w are the length and width of the FR4 platform, respectively, a is the spacing of adjacent coils, b is the width of coil, and s is the width of the exterior border zone of the platform.

Therefore, by solving Equation (1), the mechanical half deflection angle θ at resonant frequency ω_n is

$$\theta = \theta_0 \sin\left(\omega_n t - \frac{\pi}{2}\right), \tag{5}$$

where θ_0 is the amplitude of deflection angle and is calculated as

$$\theta_0 = \frac{U_{d0} B M_d Q}{K \sqrt{R_d^2 + (\omega L_d)^2}}. \tag{6}$$

Meanwhile, the moving induced electromotive force ε_s in the sensing coil can be described as

$$\varepsilon_s = B M_s \dot{\theta}, \tag{7}$$

where M_s is identified as the area sum of all the sensing coil, and it can be calculated from

$$M_s = 2 \sum_{n=1}^{N_s} \left(\left(a + \frac{3}{2}b \right) + (n-1)(a+b) \right) \cdot ((5a+7b) + 4(n-1)(a+b)) - \left(\left(a + \frac{3}{2}b \right) + (N_s-1)(a+b) \right) \cdot ((3a+4b) + 2(N_s-1)(a+b)) + \left(\frac{w}{2} - s \right) \cdot \left(\left(a + \frac{3}{2}b \right) + (N_s-1)(a+b) + \left(\frac{l}{2} - s \right) \right), \tag{8}$$

where N_s is the number of the sensing coil turns. All the aforementioned parameters are listed in Table 1.

Table 1. Main parameters of the FR4 micromirror integrated with angle sensor.

Parameters	l	w	N_d	N_s	a	b	s	Q	K	B
Value	12	12	11	9	4	4	0.5	59	0.016	100
Unit	mm	mm	-	-	mil	mil	mm	-	N·m/rad	mT

By substituting Equation (5) to Equation (7), the moving induced electromotive force ε_s in the sensing coil can be expressed as

$$\varepsilon_s = \theta_0 \omega_n B M_s \sin \omega t. \tag{9}$$

According to Equation (9), we can see that the amplitude of the moving induced electromotive force is proportional to that of the deflection angle. Moreover, it has a phase difference of $\pi/2$ with the deflection angle of the micromirror, and is in phase with the driving voltage.

However, the angle sensor output voltage consists of not only the moving-induced electromotive force but, also, the coupling voltage coupled from the driving signal. The coupling effect of the driving and sensing coils can be described as a coupled inductor model, and its equivalent circuit model is shown in Figure 2a. The resistances of the driving coil and sensing coil are 3.7Ω and 2.4Ω , respectively. In order to better analyze the coupling effect and obtain the corresponding parameters, electromagnetic field finite element analysis (FEA) of the device is performed by using the Ansoft Maxwell simulation tool. All the material properties used in the simulation are from the material library of the software. The finite element model of the mirror consisting of the FR4 substrate, driving and sensing coils, and an aluminum-coated silicon mirror plate, is shown in Figure 2b, as well as the parameters obtained through magnetostatic analysis. We can see that the coupling effect is weak, due to the small coupling coefficient ($K_c = 0.23606$). According to our previous work, the current in the driving coil is much larger than that in the sensing coil. Thus, the coupling effect of the sensing coil on the driving coil can be neglected. We only need to analyze the coupling voltage in the sensing coil coupled from the driving signal.

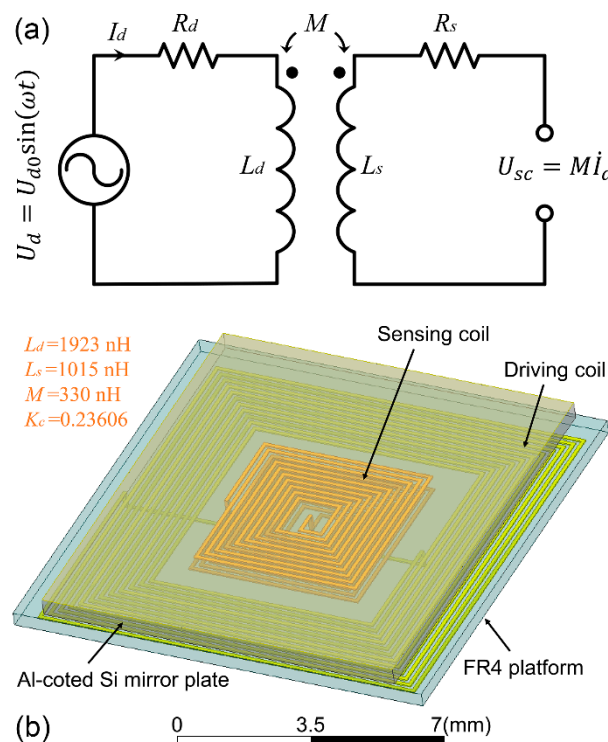


Figure 2. (a) An equivalent coupled inductor circuit model to describe the coupling effect between the driving and sensing coils. (b) Electromagnetic field finite element model of the mirror consisting of the FR4 substrate, driving and sensing coils, and an aluminum-coated silicon mirror plate, and the parameters obtained by magnetostatic analysis. R_d and R_s are the resistances, and L_d and L_s are the inductances of the driving coil and sensing coil, respectively. M is the mutual inductance between the driving and sensing coils, K_c is the coupling coefficient, and U_{sc} is the coupling voltage in the sensing coil coupled from the driving signal.

The coupling voltage U_{sc} in the sensing coil coupled from the driving signal can be expressed as

$$U_{sc} = M\dot{I}_d. \tag{10}$$

By substituting Equation (2) to Equation (10), the coupling voltage U_{sc} in the sensing coil can be given as a function of the driving voltage:

$$U_{sc} = M \frac{U_{d0}\omega}{\sqrt{R_d^2 + (\omega L_d)^2}} \sin\left(\omega t + \frac{\pi}{2}\right). \tag{11}$$

According to Equation (11), we can obtain that the amplitude of the coupling voltage in the sensing coil is proportional to that of the driving voltage. The coupling voltage in the sensing coil has a phase difference of $\pi/2$ with the driving voltage.

Therefore, while considering the coupling voltage in the sensing coil coupled from the driving signal, the output voltage U_s of the integrated angle sensor is

$$U_s = \varepsilon_s + U_{sc}. \tag{12}$$

According to Equations (6), (9), (11), and (12), the output voltage of the integrated angle sensor can be calculated as

$$U_s = \theta_0\omega \sqrt{(BM_s)^2 + \left(\frac{MK}{BM_dQ}\right)^2} \sin(\omega t + \varphi), \tag{13}$$

where

$$\varphi = \arcsin \frac{1}{\sqrt{\left(\frac{B^2M_dM_sQ}{MK}\right)^2 + 1}}, \tag{14}$$

where φ is the phase difference between the output voltage U_s and the moving-induced electromotive force ε_s . Equations (13) and (14) give the relationship of the output voltage of the sensor and the deflection angle of the micromirror considering the coupling effect in theory.

3. Experimental Results and Discussion

Figure 3a shows the schematic drawing of the measurement setup of the angle sensor. The micromirror works at the resonance point (361.8 Hz). The scan angle is controlled by adjusting the driving voltage amplitude, and can be calculated according to the length of laser scan line and the distance between the optical screen and the micromirror. The length of laser scan line can be measured accurately through a position sensitive detector (PSD). Meanwhile, the corresponding output signal of the angle sensor is amplified by a simple voltage amplifier with a gain of 400, and then measured using an oscilloscope. After this amplifier, the signal amplitude can reach a level of several hundred millivolts, which is large enough to be detected by the oscilloscope. The photograph of the real experimental setup is shown in Figure 3b. In order to measure the coupling voltage coupled from the driving signal, and keep the device virtually undamaged at the same time, we take away the magnets of the assembled micromirror, so that the mirror plate cannot move due to the absence of a magnetic field, and then excite the driving coil to see the output of the sensing coil.

Figure 4 illustrates the comparison of the driving signal, sensor output, and coupling signal in the sensing coil coupled from the driving signal in time domain. We can observe that the sensor output signal is nearly in phase with the driving signal. The small phase difference of 5.1° is caused by the superposed coupling signal in the sensing coil, and it is close to the theoretical value of 4.4° calculated by Equation (14). Meanwhile, the coupling signal in the sensing coil has a phase difference of 89.6° with the driving signal, which is also very close to the theoretical value of 90° calculated

from Equation (11). Both the minor errors between the experimental and theoretical values could be attributed to electronic noise and a little measurement error.

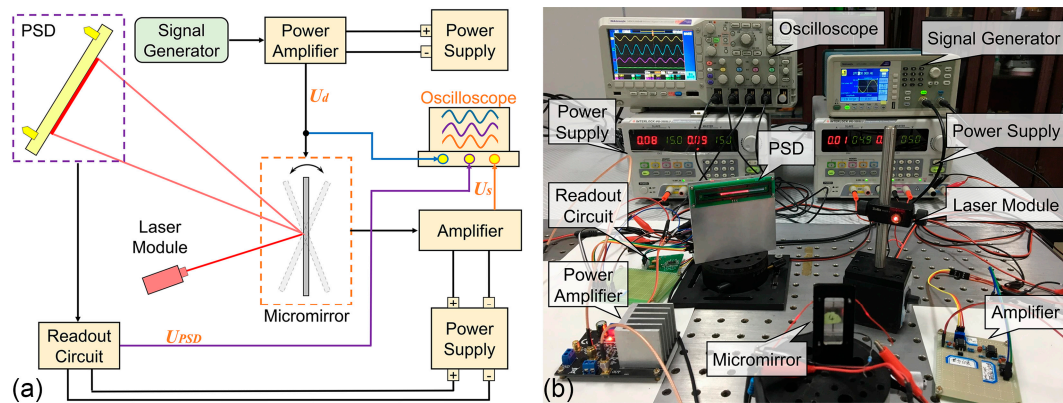


Figure 3. (a) Schematic drawing and (b) photograph of the measurement setup.

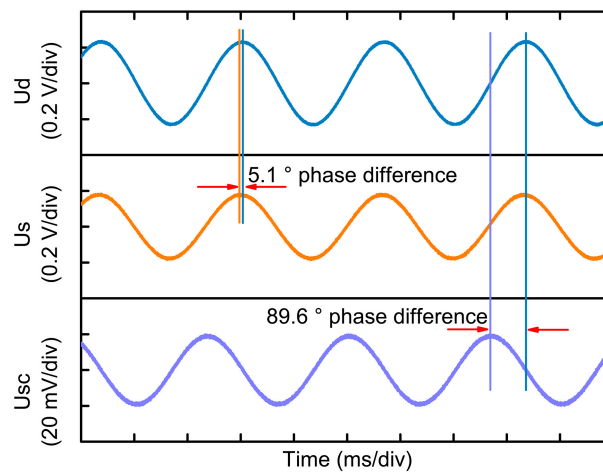


Figure 4. Comparison of the driving signal, sensor output and coupling signal in the sensing coil coupled from the driving signal in time domain.

Figure 5a plots the relationship between the coupling voltage in the sensing coil and the driving voltage. We can see that the amplitude of the coupling voltage is proportional to that of the driving voltage. The test data is in good agreement with the theoretical result obtained by Equation (11), although there is a little deviation between them. The deviation is caused by the minor error between the real and simulated mutual inductances. Owing to the difference between the real and simulated material parameters, the simulated mutual inductance inevitably deviates a little from the real value.

According to Figure 5b, we can see a clear linear relationship between the sensor output voltage and the optical scan angle of the micromirror. The correlation coefficient r can reach 0.9995. This is well consistent with the theoretical relation determined by Equation (13). The sensitivity of the angle sensor can be determined as $55.0 \text{ mV}_p/\text{^\circ}$, which is also very close to the theoretical value of $55.2 \text{ mV}_p/\text{^\circ}$, calculated by Equation (13). The difference between the experimental and theoretical values can be attributed to the process error. In addition, a little nonlinear behavior of the test result is observed in Figure 5b. It is caused by the coupling effect between the driving and sensing coils. By comparing Equation (9) with (13), we can find that the parameter of torsional stiffness K is introduced in Equation (13) when considering the coupling voltage in the sensing coil coupled from the driving signal. Owing to the nonlinear spring effect of the torsion bars [15,24], K is not a constant, but varies with the change of the scan angle. Thus, a little nonlinear behavior of the test result is observed. The theoretical result is perfectly linear because K is assumed to be a constant in the theoretical calculation.

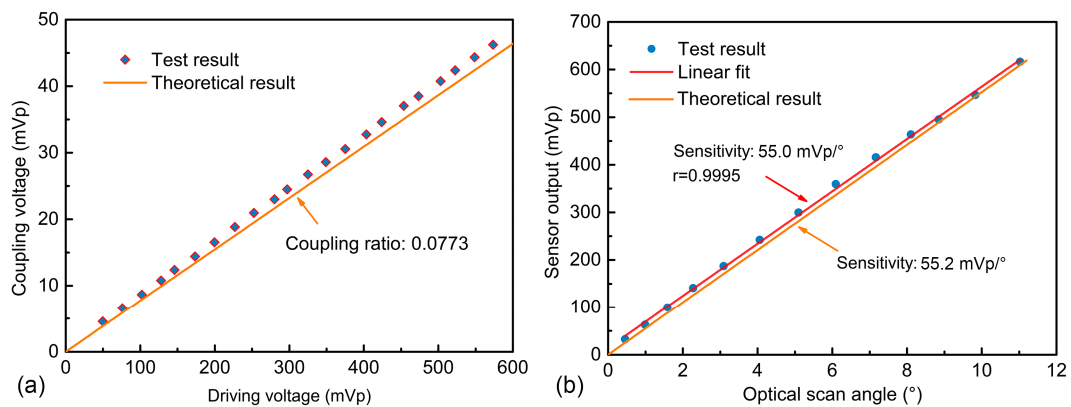


Figure 5. (a) Relation between the coupling voltage in the sensing coil and the driving voltage. (b) Relation between the sensor output and the optical scan angle. Note: all the voltage values are measured as peak value.

The frequency spectrum from 0 to 800 Hz (surrounding the 361.8 Hz) was measured to identify the signal-to-noise ratio (SNR) of the angle sensor. In this test, the sensor signal is recorded in the oscilloscope after going through the aforementioned amplifier and a fourth-order bandpass filter. Then, the frequency spectrum can be obtained through a fast Fourier transform of the time-domain signal. Figure 6a,b show the measured frequency spectrum at the optical scan angle of 4.6°, and the corresponding angle sensor output in time domain, respectively. This signal shows a great signal quality of 71.9 dB SNR, which is beneficial for feedback control.

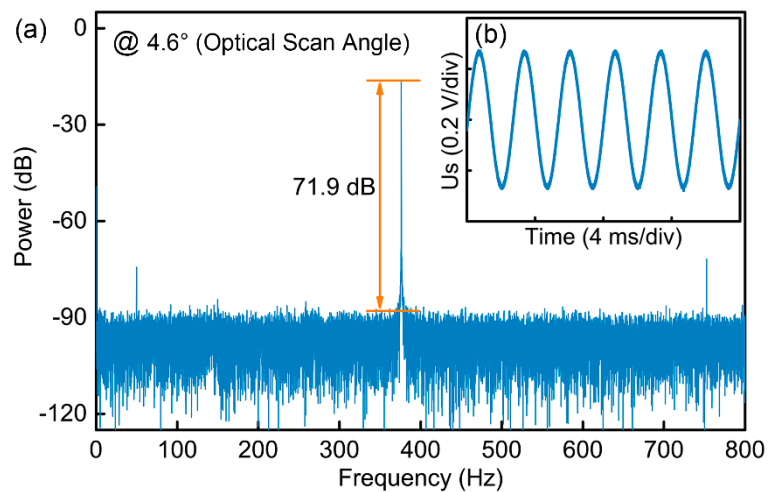


Figure 6. (a) Frequency spectrum of the sensor output at the optical scan angle of 4.6°. (b) The corresponding signal in time domain.

Figure 7 shows the frequency characteristics of the angle sensor compared to the optical scan angle obtained from PSD measurement. In the measurement, the micromirror is actuated by the sinusoidal sweep signal from 348 Hz to 378 Hz. The frequency response functions of the micromirror are measured by the angle sensor and PSD, respectively. We can see that two frequency response functions have almost the same overall profile, which means that the angle sensor can still work, even though the micromirror is off the resonance. In addition, the phase curve in Figure 7 shows that the phase of the sensor output voltage will change when the micromirror oscillates off the resonance. Therefore, the resonance can be tracked by monitoring the phase difference between the sensor output and driving signals, i.e., a phase-lock loop [21].

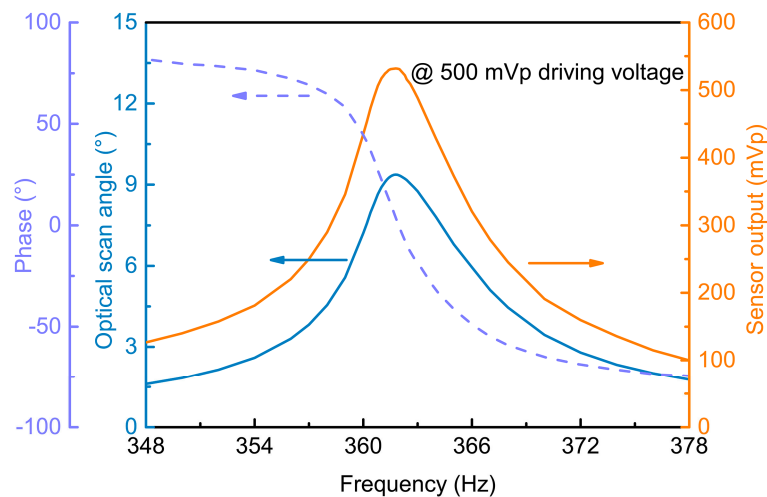


Figure 7. Frequency response function of the micromirror measured by the angle sensor and position sensitive detector (PSD) and phase curve of the angle sensor. The phase represents the phase difference between the sensor output and driving voltage.

Based on the great angle sensor signal quality, a simple closed-loop control circuit was developed to further verify the sensor's good feasibility for feedback control. Figure 8a demonstrates the closed-loop control scheme. The micromirror is actuated to oscillate around the torsion bars by the sinusoidal driving signal. Meanwhile, the generated sinusoidal angle sensor signal, depending on the deflection angle of the micromirror, is detected by the angle sensor signal acquisition module. After going through the rectifier-filter module, the signal is converted to a DC voltage signal. To stabilize the deflection angle, the amplitude gain control module was introduced. The signal of the voltage difference between the DC voltage, representing the deflection angle and the reference voltage signal, is input to the module. Then, the amplitude gain control is mainly accomplished by multiplying the voltage difference with the sinusoidal signal generated by signal generation module. Therefore, the amplitude of the driving signal can be regulated in real time according to the feedback signal of the integrated angle sensor.

Long-term stability tests on the micromirror were operated continuously for 12 h, both with and without closed-loop control. Figure 8b shows the test result. The maximum variations of the optical scan angle are 3.04% and 7.83%, respectively. Hence, the micromirror operated with closed-loop control possesses better long-term stability. This result indicates the angle sensor's good feasibility for feedback control.

Finally, temperature stabilities of the micromirror, operated both with and without closed-loop control, were also tested. In this test, the micromirror is placed in a high and low temperature test chamber. The temperature is increased from 20 to 50 °C in increments of 5 °C under atmospheric pressure. The test result is shown in Figure 9. With the change of temperature, the resonant frequency of the device varies, and the micromirror will work off the resonance [21,25]. Hence, we can see that the optical scan angle decreases with the increase of temperature. Without closed-loop control, the optical scan angle decreases from 4.6° to 1° as the temperature rises from 20 to 50 °C. On the other hand, with closed-loop control, the optical scan angle decreases from 4.6° to 2.5°. By comparison, the micromirror operated with closed-loop control possesses relatively better temperature stability. It indicates that the feedback control, based on the integrated angle sensor, is workable and is beneficial to improve the micromirror's temperature stability. However, due to the limited adjustable voltage range of this analog closed-loop control circuit, and the lack of tracking-resonance function, the maximum variation of scan angle still reaches 45.65%. Therefore, it is highly desirable to develop a more precise digital closed-loop control circuit that can regulate the amplitude and frequency of the driving signal in follow-up work.

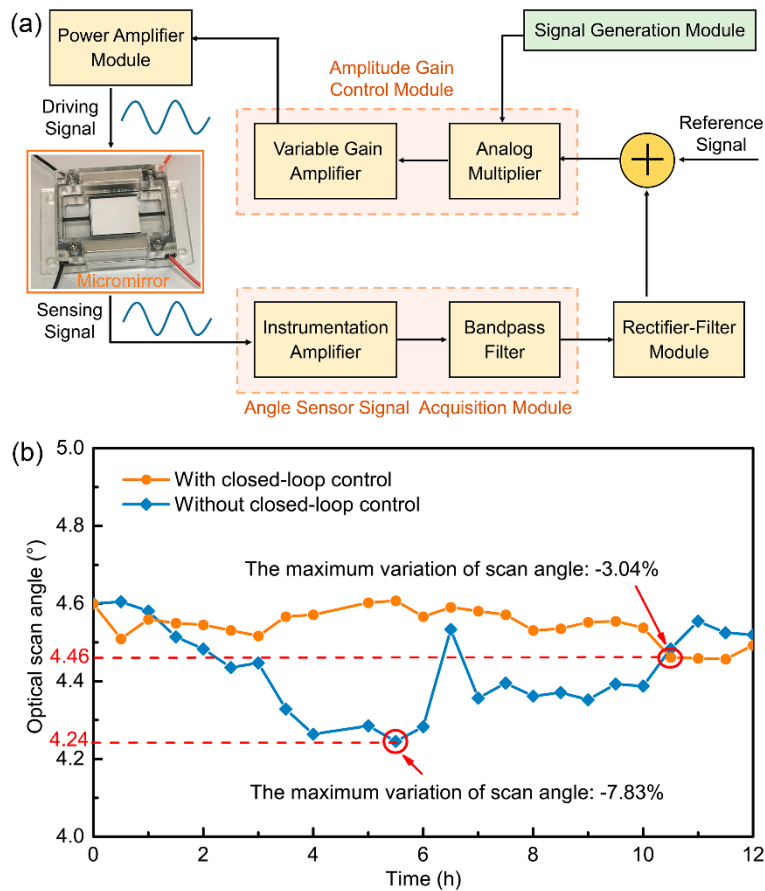


Figure 8. Closed-loop control: (a) Block diagram of the closed-loop control for the FR4 micromirror. (b) Comparison of long-term stabilities for the FR4 micromirror operated with closed-loop control and without closed-loop control.

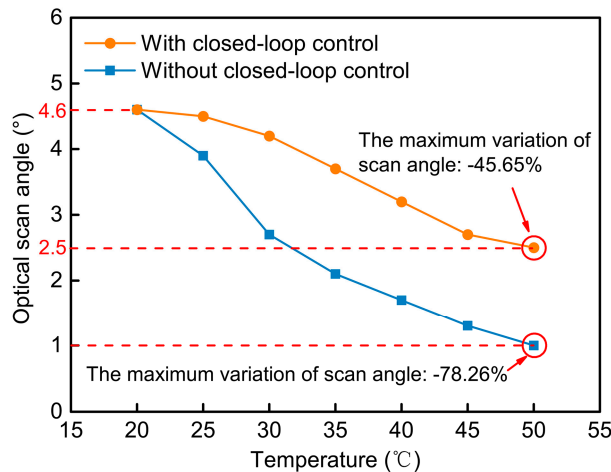


Figure 9. Comparison of temperature stabilities for the FR4 micromirror operated with closed-loop control and without closed-loop control.

4. Conclusions

In this work, an electromagnetic angle sensor integrated in the FR4-based micromirror is investigated in detail. An accurate theoretical model was developed to predict the sensor output, especially considering the coupling effect between the driving and sensing coils. The coupling parameters (i.e., inductances of the driving coil and sensing coil, mutual inductance, and coupling

coefficient) in the model were obtained by electromagnetic field FEA simulation. Test results of the coupling voltage in the sensing coil and the sensor output are in good agreement with the theoretical results, which indicates the high accuracy of the theoretical model. Although the coupling effect of the driving coil on the sensing coil affects the linearity of the angle sensor, it can still reach 0.9995. Moreover, the integrated angle sensor has a sensitivity of $55.0 \text{ mV}_p/^\circ$ and a high SNR of 71.9 dB. Additionally, the frequency response and phase-frequency characteristics of the angle sensor are also measured and discussed. Finally, the sensor's good feasibility for feedback control has been verified through a simple closed-loop control circuit. Experimental results show that the micromirror operated with closed-loop control possesses better long-term stability and temperature stability than that operated without closed-loop control. In the future, the long-term stability and temperature stability of the micromirror can be further improved by developing a more precise digital closed-loop control circuit.

Author Contributions: Q.W., H.L. and Z.W. conceived and designed the integrated angle sensor; H.L., F.Y. and D.L. deduced the theory; H.L., Y.S., J.H. and L.H. performed the experiments and analyzed the data; H.L. and F.Y. conceived and developed the closed-loop control circuit; Q.W. and H.L. wrote the paper; Z.W. revised it.

Funding: This research was funded by the National Key R&D Program of China (Grant No. 2018YFF01011200), the Special Funds of the National Natural Science Foundation of China (Grant No. 61327002), the National Natural Science Foundation of China (Grant No. 61804016) and the Fundamental Research Funds for Central Universities (Grant No. 106112017CDJXY120006).

Acknowledgments: The authors want to thank Xiaokang Yang, Chao Yang and Shan Lu for their valuable advice about the experiments.

Conflicts of Interest: The authors declare no conflict of interest.

References

1. Yalcinkaya, A.D.; Ergeneman, O.; Urey, H. Polymer magnetic scanners for bar code applications. *Sens. Actuators A Phys.* **2007**, *135*, 236–243. [[CrossRef](#)]
2. Duan, C.; Tanguy, Q.; Pozzi, A.; Xie, H. Optical coherence tomography endoscopic probe based on a tilted mems mirror. *Biomed. Opt. Express* **2016**, *7*, 3345–3354. [[CrossRef](#)] [[PubMed](#)]
3. Ito, K.; Niclass, C.; Aoyagi, I.; Matsubara, H.; Soga, M.; Kato, S.; Maeda, M.; Kagami, M. System design and performance characterization of a mems-based laser scanning time-of-flight sensor based on a 256×64 -pixel single-photon imager. *IEEE Photonics J.* **2013**, *5*, 6800114. [[CrossRef](#)]
4. Ye, L.; Zhang, G.; You, Z. Large-aperture khz operating frequency ti-alloy based optical micro scanning mirror for lidar application. *Micromachines* **2017**, *8*, 120. [[CrossRef](#)]
5. Wang, Y.; Gokdel, Y.D.; Triesault, N.; Wang, L.; Huang, Y.Y.; Zhang, X. Magnetic-actuated stainless steel scanner for two-photon hyperspectral fluorescence microscope. *J. Microelectromech. Syst.* **2014**, *23*, 1208–1218. [[CrossRef](#)]
6. Jeong, H.M.; Park, Y.H.; Lee, J.H. Slow scanning electromagnetic scanner for laser display. *J. Microlithogr. Microfabr. Microsyst.* **2008**, *7*, 1589–1604.
7. Zuo, H.; He, S. Fpcb micromirror-based laser projection availability indicator. *IEEE Trans. Ind. Electron.* **2016**, *63*, 3009–3018. [[CrossRef](#)]
8. Ataman, Ç.; Urey, H. Compact fourier transform spectrometers using fr4 platform. *Sens. Actuators A Phys.* **2009**, *151*, 9–16. [[CrossRef](#)]
9. Zhou, Y.; Wen, Q.; Wen, Z.; Huang, J.; Chang, F. An electromagnetic scanning mirror integrated with blazed grating and angle sensor for a near infrared micro spectrometer. *J. Micromech. Microeng.* **2017**, *27*, 125009. [[CrossRef](#)]
10. Huang, J.; Wen, Q.; Nie, Q.; Chang, F.; Zhou, Y.; Wen, Z. Miniaturized nir spectrometer based on novel moems scanning tilted grating. *Micromachines* **2018**, *9*, 478. [[CrossRef](#)] [[PubMed](#)]
11. Namazu, T.; Isono, Y. Fatigue life prediction criterion for micro–nanoscale single-crystal silicon structures. *J. Microelectromech. Syst.* **2009**, *18*, 129–137. [[CrossRef](#)]
12. Urey, H.; Holmstrom, S.; Yalcinkaya, A.D. Electromagnetically actuated fr4 scanners. *IEEE Photonics Technol. Lett.* **2007**, *20*, 30–32. [[CrossRef](#)]

13. Zuo, H.; He, S. Fpcb ring-square electrode sandwiched micromirror based laser pattern pointer. *IEEE Trans. Ind. Electron.* **2017**, *64*, 6319–6329. [[CrossRef](#)]
14. Zuo, H.; He, S. Double stage fpcb scanning micromirror for laser line generator. *Mechatronics* **2018**, *51*, 75–84. [[CrossRef](#)]
15. Lei, H.; Wen, Q.; Yu, F.; Zhou, Y.; Wen, Z. FR4-based electromagnetic scanning micromirror integrated with angle sensor. *Micromachines* **2018**, *9*, 214. [[CrossRef](#)] [[PubMed](#)]
16. Han, F.; Wang, W.; Zhang, X.; Xie, H. Modeling and control of a large-stroke electrothermal mems mirror for fourier transform microspectrometers. *J. Microelectromech. Syst.* **2016**, *25*, 750–760. [[CrossRef](#)]
17. Han, F.T. Miniature fourier transform spectrometer with a dual closed-loop controlled electrothermal micromirror. *Opt. Express* **2016**, *24*, 22651. [[CrossRef](#)] [[PubMed](#)]
18. Sasaki, M.; Tabata, M.; Haga, T.; Hane, K. Piezoresistive rotation angle sensor integrated in micromirror. *Jpn. J. Appl. Phys.* **2006**, *45*, 3789–3793. [[CrossRef](#)]
19. Chi, Z.; Zheng, Y.; Hu, H.; Li, G. Study on a two-dimensional scanning micro-mirror and its application in a moems target detector. *Sensors* **2010**, *10*, 6848–6860.
20. Park, Y.H. Low power and highly precise closed-loop driving circuits for piezoelectric micromirrors with embedded capacitive position sensors. In *MOEMS and Miniaturized Systems XV*; SPIE Press: Bellingham, WA, USA, 2016.
21. Naono, T.; Fujii, T.; Esashi, M.; Tanaka, S. A large-scan-angle piezoelectric mems optical scanner actuated by a nb-doped pzt thin film. *J. Micromech. Microeng.* **2013**, *24*, 5010. [[CrossRef](#)]
22. Gu-Stoppel, S.; Giese, T.; Quenzer, H.J.; Hofmann, U.; Benecke, W. Piezoelectrically driven and sensed micromirrors with large scan angles and precise closed-loop control. In Proceedings of the MikroSystemTechnik 2017 Congress, Munich, Germany, 23–25 October 2017; p. 561.
23. Watanabe, Y.; Kobayashi, S.; Iwamatsu, S.; Yahagi, T.; Sato, M.; Oizumi, N. Motion monitoring of mems actuator with electromagnetic induction. *Electron. Commun. Jpn.* **2014**, *97*, 52–57. [[CrossRef](#)]
24. Kundu, S.K.; Ogawa, S.; Kumagai, S.; Fujishima, M.; Hane, K.; Sasaki, M. Nonlinear spring effect of tense thin-film torsion bar combined with electrostatic driving. *Sens. Actuators A Phys.* **2013**, *195*, 83–89. [[CrossRef](#)]
25. Ishikawa, N.; Ikeda, K.; Sawada, R. Temperature dependence of the scanning performance of an electrostatic microscanner. *J. Micromech. Microeng.* **2016**, *26*, 035002. [[CrossRef](#)]



© 2018 by the authors. Licensee MDPI, Basel, Switzerland. This article is an open access article distributed under the terms and conditions of the Creative Commons Attribution (CC BY) license (<http://creativecommons.org/licenses/by/4.0/>).